Electrostatic–magnetic hybrid ion acceleration for high-thrust-density operation

🆔 D. Ichihara, R. Nakano, 🆔 Y. Nakamura, et al.

COLLECTIONS

Paper published as part of the special topic on Physics of Electric Propulsion

View Online   Export Citation   CrossMark

ARTICLES YOU MAY BE INTERESTED IN

Electrostatic–magnetic hybrid ion acceleration for high-thrust-density operation

View Online   Export Citation   CrossMark

D. Ichihara,[a] R. Nakano, Y. Nakamura, K. Kinefuchi, and A. Sasoh

AFFILIATIONS

Department of Aerospace Engineering, Nagoya University, Nagoya, Aichi 464-8603, Japan

Note: This paper is part of the Special Topic on Physics of Electric Propulsion.
[a]**Author to whom correspondence should be addressed:** daisuke.ichihara@mae.nagoya-u.ac.jp

ABSTRACT

To achieve high-thrust-density operation, we propose electrostatic–magnetic hybrid ion acceleration in which the empirical thrust density limit of the electrostatic acceleration is surpassed without violent plasma oscillation by combing the collisional momentum transfer mechanism, which is the ion acceleration mechanism of the electromagnetic acceleration. To achieve hybrid ion acceleration, we experimentally obtained two design criteria: one near anode propellant injection and another at the on-axis hollow cathode location. The thrust characteristics of three thrusters composed of a slowly diverging magnetic field between an on-axis hollow cathode and a coaxially set ring anode were examined. By injecting xenon propellant along the anode inner surface, the electron impact ionization process was enhanced, and generated ions are electrostatically accelerated through the radial-inward potential gradient perpendicular to the axial magnetic lines of force. The hybrid ion acceleration characteristics were obtained only if these two criteria were satisfied and the obtained thrust was consistent with the thrust formula derived for steady-state, quasi-neutral plasma flows. In addition to the criteria, strengthening the magnetic field and enhancing the propellant mass flux were effective for improving thrust density without deteriorating thrust efficiency. Among the experimental conditions in this study, the maximum thrust density was $70\,\text{N/m}^2$ with an anode specific impulse of 1200 s, which cannot be achieved in a purely electrostatic thruster with thrust density 6.3 times than that of a typical Hall thruster.

I. INTRODUCTION

Compared to chemical propulsion, electric propulsion has the advantage of high specific impulse, and the usefulness of electric propulsion has been demonstrated in numerous missions.[1] Based on the energy conversion law, thrust and specific impulse have opposite dependences on the propellant mass flow rate, given a constant power.[2] This relationship between specific impulse and thrust should cause each to offset the other in the trade-off between payload mass and working period. Specifically, larger satellites for orbit riding in all-electric satellite,[3] space-debris removal,[4] or Mars cargo/piloted-class missions[5] require a higher thrust density because short travel time is prioritized,[6] and a smaller thrust density requires more time to attain a certain velocity increment. Because the available thrust is proportional to thrust density, thrust density is one of the most important factors[7] to reduce the satellite mass as much as possible.[8] Regarding electric space propulsions, the plasma acceleration principle is typically divided into three types, namely, electrostatic, electromagnetic, and electrothermal accelerations.[9] In electrostatic-acceleration-type

thrusters, the ions can gain energy corresponding to the applied voltage, and the electrostatic thrust density is proportional to propellant mass flux. In ion thrusters,[1] only the ions experience a propulsive force, which is the thrust between several grids having different electrical potentials, while the electrons are not introduced within the grids. This configuration is favorable for obtaining high-thrust efficiency because by employing appropriate beam optics, collision-less momentum transfer is realized. However, the thrust density is limited due to Child–Langmuir's space-charge limit.[10] Considering the existing data, the thrust densities of the state-of-the-art ion engines are $3.8\,\text{N/m}^2$ for T6[11] or $3.3\,\text{N/m}^2$ for XIPS-25.[12] Further, in Hall thrusters,[13] and other similar types of thrusters such as cylindrical Hall thrusters,[14] high-efficiency multistage plasma (HEMP) thrusters,[15] and diverging-magnetic-field electrostatic thrusters,[16] the ions are accelerated in quasi-neutral plasma such that Child–Langmuir's law does not limit the thrust density. Raitses and Fisch[17] suggested a theoretical thrust density limitation based on Ampère's circuital law wherein the maximum thrust density is proportional to the magnetic

pressure $B_m^2/(2\mu)$; B_m is the maximum magnetic field strength inside the acceleration region, and μ is the magnetic permeability. For current Hall thrusters operating in the power range of 0.5–10 kW with $B_m \approx 10$–30 mT, the theoretical thrust density limit is calculated as 100–400 N/m². In practice, the available thrust densities in the state-of-the-art Hall thrusters are 10 N/m² for SPT-100[18] and 20 N/m² for nested Hall thruster X-3[19] because both electron collisions and scattering on oscillations might produce electron current losses and large beam divergence. Li et al.[20] reported thrust density improvement in a Hall thruster with a variable discharge channel consisting of an inner divergent annular segment and a cylindrical segment near the exit. By supplying propellant along the channel centerline, a thrust density of 23 N/m² was achieved. Dannenmayer and Mazouffre[21] suggested an optimum propellant mass flux considering the fact that a smaller mass flux results in insufficient propellant ionization, whereas a larger mass flux leads to deterioration in thrust efficiency because of excessive electron cross-field transport by collisions. To decouple the propellant ionization and acceleration, a double stage Hall thruster, with an inductively coupled plasma source between the anode and cathode, was proposed.[22] The preliminary experimental results suggested that the expected thrust density was half that of the conventional Hall thrusters, and the estimated thrust efficiency deteriorated with an increase in the plasma source power.

In contrast, in electromagnetic-acceleration-type thrusters such as magnetoplasmadynamic thrusters,[23] the quasi-neutral plasma experiences a Lorentz force generated by the interactions between the discharge current and applied- and/or self-induced magnetic field. As most of the discharge current is carried by the electrons, a momentum transfer mechanism from the electrons to ions is required. If such momentum transfer is caused by particle collisions, the ions can obtain a kinetic energy greater than that corresponding to the discharge voltage.[24] Therefore, the thrust density can be higher than that of the Hall thrusters. However, such collisional momentum transfer is accompanied by poor energy transfer efficiency as well as poor thrust efficiency. In electrothermal-acceleration-type thrusters, which are often represented by arcjet thrusters,[25] the propellant gains propulsive kinetic energy from Joule heating. In this case, high thrust density can be achieved, with modest thrust efficiency. In summary, electrostatic- or electromagnetic-acceleration-type thrusters have a theoretical and/or empirical limitation for thrust density. Several challenges remain, which need to be overcome to improve the thrust density without deteriorating thrust efficiency.

In the above-mentioned categorization, the electrostatic and electromagnetic acceleration are regarded as different types. Sasoh et al.[26] experimentally demonstrated the thrust characteristics exhibiting both electrostatic and electromagnetic features in the thruster that comprises a slowly diverging magnetic field between an on-axis central cathode and a coaxially set ring anode. We refer to this ion acceleration method as electrostatic–magnetic hybrid ion acceleration. As we mentioned above, the electrostatic acceleration shows a higher thrust efficiency but a limited thrust density due to the plasma oscillations, whereas the electromagnetic acceleration shows the opposite trend due to the energy dissipation in the collisional process. In the hybrid acceleration, the electrostatic–magnetic hybrid acceleration mechanism has an expected potential to achieve both high thrust efficiency and high thrust density

without plasma oscillations by combing the advantages of each acceleration process: however, such a hybrid thrust generation has not been well recognized as a promising method in electric space propulsion. To further investigate this technology, the respective thrust components, electrostatic and electromagnetic, must be quantified. In this study, we briefly describe the fundamental equations of the electrostatic–magnetic hybrid ion acceleration and related thrust formulas. Thereafter, the criteria regarding propellant injection scheme and hollow cathode position for realization of the hybrid ion acceleration are discussed based on the experimentally obtained thrust and plasma parameters. Moreover, by supplying a high propellant mass flux, we also demonstrated the high thrust density that cannot be achieved in a purely electrostatic or electromagnetic acceleration method.

II. THRUST FORMULA IN HYBRID ION ACCELERATION

In this section, the fundamental equations of the electrostatic–magnetic hybrid ion acceleration and related thrust formulae are briefly described. The detailed mathematical formulation procedures can be found in our previous report.[27] We start with the steady-state Euler equation for axisymmetric, single fluid plasma, as follows:

$$\rho(\mathbf{u} \cdot \nabla \mathbf{u}) = -\nabla p + \mathbf{j} \times \mathbf{B}, \tag{1}$$

where ρ, $\mathbf{u}$, p, $\mathbf{j}$, and $\mathbf{B}$ are mass density, velocity vector, pressure tensor, current density vector, and magnetic field vector, respectively. In the following formulation, the first term on the right-hand side in Eq. (1) is neglected because in high specific impulse operation, the contribution of electrothermal acceleration is much smaller than the second term $\mathbf{j} \times \mathbf{B}$. Further, the ion velocity can be divided into the translational and azimuthal components: $\mathbf{u} = \mathbf{u}_{r,z} + \mathbf{u}_\theta$, where $\mathbf{u}_{r,z} \equiv (u_r, 0, u_z)$ and $\mathbf{u}_\theta \equiv (0, u_\theta, 0)$. For cylindrical coordinates (r, θ, z), the convective acceleration term on the left-hand side of Eq. (1) is arranged as follows by using the Lagrangian derivative D/Dt:

$$\mathbf{u} \cdot \nabla \mathbf{u} = \left(\frac{Du_r}{Dt} - \frac{u_\theta^2}{r}, \quad \frac{Du_\theta}{Dt} + \frac{u_r u_\theta}{r}, \quad \frac{Du_z}{Dt} \right). \tag{2}$$

Neglecting the self-induced magnetic field B_θ, the magnetic field vector consists of only the applied component $B = B_a = (B_r, 0, B_z)$. The current density vector $\mathbf{j}$ is the sum of the discharge current $\mathbf{j}_d \equiv (j_r, 0, j_z)$ and that induced from the $E \times B$ electron motion $\mathbf{j}_i \equiv (0, j_\theta, 0)$. The induced current is proportional to the discharge current via the proportional coefficient of α_{ES}, $|\mathbf{j}_i| = \alpha_{ES}|\mathbf{j}_d|$. Combining Eqs. (1) and (2) with the above-mentioned assumptions, the following expressions are obtained:

$$\frac{1}{2}\rho \frac{Du_{r,z}^2}{Dt} = (\mathbf{j}_i \times \mathbf{B}_a) \cdot \mathbf{u}_{r,z} + \rho \frac{u_r u_\theta^2}{r}, \tag{3}$$

$$\frac{1}{2}\rho \frac{Du_\theta^2}{Dt} = (\mathbf{j}_d \times \mathbf{B}_a) \cdot \mathbf{u}_\theta - \rho \frac{u_r u_\theta^2}{r}. \tag{4}$$

Equation (3) implies that the kinetic energy of the translational motion is gained via the work done by an apparent Lorentz force, $\mathbf{j}_i \times \mathbf{B}_a$, in the direction of $\mathbf{u}_{r,z}$, which indicates an electrostatic

acceleration. Here, the interaction between the induced azimuthal current $\mathbf{j}_i$ and the applied magnetic field $\mathbf{B}_a$ is a generalized form of Hall acceleration,[24] which is equivalent to the electrostatic acceleration. Similarly, based on Eq. (4), the kinetic energy of the swirl motion is gained via the work done by the Lorentz force, $\mathbf{j}_d \times \mathbf{B}_a$, in the azimuthal direction, which indicates an electromagnetic (normally referred to as "Swirl"[28]) acceleration. Such kinetic energies are exchangeable via the work done against a centrifugal force, $\rho u_\theta^2/r$. Overall, the total kinetic energy equation is the sum of the works done by the resultant Lorentz force,

$$\frac{1}{2}\rho\frac{Du^2}{Dt} = (\mathbf{j}_i \times \mathbf{B}_a) \cdot \mathbf{u}_{r,z} + (\mathbf{j}_d \times \mathbf{B}_a) \cdot \mathbf{u}_\theta. \quad (5)$$

Therefore, the exhaust velocity U is acquired by integrating the left-hand side of Eq. (5) in the control volume (CV), which has a radius of R_a and an effective length of L,

$$\int_{CV}\frac{1}{2}\rho\frac{Du^2}{Dt}dV = \frac{1}{2}\dot{m}U^2. \quad (6)$$

To obtain U and thrust F, Eqs. (5) and (6) are calculated by using the effective coefficients. Hereafter, the bar over a quantity denotes the representative value in CV. For electrostatic acceleration, the volume integration is calculated as

$$\int_{CV}(\mathbf{j}_i \times \mathbf{B}_a) \cdot \mathbf{u}_{r,z}dV = \alpha_{ES}\bar{j}_d\bar{B}_a\bar{u}_{r,z} \cdot \pi R_a^2 L$$
$$= \alpha_{ES}\frac{J_d}{2\pi LR_a/2}\bar{B}_a\frac{U}{2} \cdot \pi R_a^2 L$$
$$= \frac{\alpha_{ES}}{2}J_d\bar{B}_a UR_a. \quad (7)$$

In contrast, for electromagnetic acceleration, it is

$$\int_{CV}(\mathbf{j}_d \times \mathbf{B}_a) \cdot \mathbf{u}_\theta dV = \bar{j}_d\bar{B}_a\bar{u}_\theta \cdot \pi R_a^2 L$$
$$= \frac{J_d}{2\pi LR_a/2}\bar{B}_a\alpha_{EM}\frac{U}{2} \cdot \pi R_a^2 L$$
$$= \frac{\alpha_{EM}}{2}J_d\bar{B}_a UR_a, \quad (8)$$

where we assume $\bar{j}_d$ is the value at $r = R_a/2$ such that $\bar{j}_d = J_d/(2\pi LR_a/2)$,[29] $\bar{u}_{r,z} = U/2$, and $\bar{u}_\theta = \alpha_{EM}U/2$. Substituting Eqs. (7) and (8) into Eq. (5), we obtain

$$\frac{1}{2}\dot{m}U^2 = \frac{\alpha_{ES}}{2}J_d\bar{B}_a UR_a + \frac{\alpha_{EM}}{2}J_d\bar{B}_a UR_a. \quad (9)$$

As a result, the thrust is expressed in an electromagnetic form as

$$F = \dot{m}U = (\alpha_{ES} + \alpha_{EM})J_d\bar{B}_a R_a = \alpha J_d\bar{B}_a R_a. \quad (10)$$

Here, the coefficient α is sum of the coefficients of α_{ES} and α_{EM}, that is, $\alpha \equiv \alpha_{ES} + \alpha_{EM}$. Equation (10) represents a traditional

electromagnetic acceleration form used for magnetoplasmadynamic thrusters; the thrust is expressed using J_d and B_a, and not explicitly using propellant mass flow rate $\dot{m}$.

Next, let F be expressed as a function of $\dot{m}$ and V_d that typically used an electrostatic thrust form in ion and Hall thrusters. The azimuthal current induced by the $E \times B$ drift of electrons is expressed as

$$j_\theta = en\bar{E}/\bar{B}_a = \alpha_{ES}\bar{j}_d = \alpha_{ES}J_d/(2\pi LR_a/2). \quad (11)$$

As $\bar{E}$ can be expressed as $\bar{E} = \beta_1 V_d/R_a$, and $\dot{m} = mn\bar{u}_z\pi R_a^2 = mn\beta_2 U\pi R_a^2$, the thrust expression in an electrostatic acceleration form is obtained using Eqs. (10) and (11) as

$$F = \dot{m}U = (\alpha_{ES} + \alpha_{EM})en\frac{\bar{E}}{\bar{B}_a}\frac{\pi R_a L}{\alpha_{ES}}\bar{B}_a R_a = \alpha'\dot{m}\sqrt{eV_d/m}, \quad (12)$$

$$\alpha' \equiv \sqrt{\left(1 + \frac{\alpha_{EM}}{\alpha_{ES}}\right)\frac{\beta_1}{\beta_2}\frac{L}{R_a}}, \quad (13)$$

where the thrust is expressed using $\dot{m}$ and V_d, and not explicitly using B_a. In Secs. IV A and IV B experimentally, obtained thrust characteristics will be fit using Eqs. (10) and (12) to investigate the electrostatic–magnetic ion acceleration performances.

III. EXPERIMENTAL SETUP

A. Thruster heads and operating conditions

In this study, we analyze experimental data obtained from three thrusters, namely, types-I, II, and III. All the thrusters have axisymmetric configurations composed of a hollow cathode on the center axis and a ring anode made of copper surrounding it. Further, only for the type-II thruster, the external cathode operation was also evaluated. The electrodes are separated by a ceramic insulator. An external magnetic field is applied using either a water-cooled solenoid coil or a permanent magnet. Further, the cylindrical coordinates (z, r) (where z and r are the axial and radial coordinates, respectively) were defined according to an axisymmetric configuration, with their origin located at the center of the ring anode (see schematic illustrations for each thruster). The strength of the applied magnetic field is represented by the value at the origin, B_c. To enhance the thrust density, we applied as strong a magnetic field as possible by using a water-cooled solenoid coil (thruster type-I) or a permanent magnet with yokes (thruster types-II and III) because the electromagnetic thrust is proportional to the magnetic field strength.[28]

The thruster operating conditions are summarized in Table I. For all three thrusters, operation with argon (gas purity of 99.999%) was examined, resulting in unstable operation and poor thrust performance. Consequently, the thrust characteristics of only xenon (gas purity greater than 99.995%) were evaluated in this study. Moreover, the same species as that of the propellant was used as the working gas of the hollow cathode, whose two positions (central or external) were examined. The uncertainty of B_c, anode mass flow rate $\dot{m}_a$, discharge voltage V_d, and discharge current J_d were ±1% (the specification of the Gausses meter, A301, Denshijiki

TABLE I. Operating conditions for thruster types-I, II, and III.

Thruster type ...	Cathode location ...	R_a mm	B_c mT	$\dot{m}_a$ mg/s	$\dot{m}_a$ Aeq	$\dot{m}_c$ mg/s	$\dot{m}_c$ Aeq	V_d V	J_d A	P_a kW	S_{out} m^2
I	Central	40	100, 125, 150	1.4	1.0	0.49	0.36	100–300	1.3–6.0	0.1–1.8	6.3×10^{-3}
II	Central	15	210, 315, 402	0.7–4.8	0.5–3.5	0.49	0.36	100–300	1.5–9.8	0.2–2.0	0.9×10^{-3}
	External	15		0.7–4.1	0.5–3.0			200–450	0.8–9.0	0.3–2.6	
III	Central	15	270	2.0–6.1	1.5–4.5	0.49	0.36	200–500	2.3–9.8	0.7–2.7	1.0×10^{-3}

Industry Co., Ltd.), $\pm 4.4 \times 10^{-2}$ mg/s ($= \pm 3.0 \times 10^{-2}$ Aeq), ± 2.0 V, and ± 51 mA, respectively. Each operating condition was repeated at least three times. In the following figures (Figs. 2, 3, 5, 7, 9, 10, and 11). a symbol shows an averaged value and the error bars represent the standard deviation ($\pm \sigma$) obtained after a number of trials with each operating condition (see Table I).

B. Vacuum facility, thrust measurement, and plasma diagnostics

In this section, we briefly describe the experimental environments of the vacuum facility, thrust measurement, and plasma diagnostics system. The details of the equipment used are described in our previous reports.[30,31] All experiments were conducted in a stainless steel (ISO: 4301-304-00-I) vacuum chamber with an inner diameter of 1.2 m and a length of 3.2 m. The vacuum chamber was evacuated from atmospheric pressure to less than 10 Pa using a dry pump (a pumping speed of 120 l/s) followed by an evacuation to the order of 10^{-4} Pa using a cryopump (a pumping speed of 8400 l/s). The base pressure of the system was 6.0×10^{-4} Pa.

The thruster was mounted on a pendulum-type thrust stand with a 300-mm-long stand arm supported by a two-knife-edge fulcrum. The knife edge was made of stainless steel (ISO: 4301-304-00-I), with a width of 10 mm and an apex angle of 90°. Each knife edge was mounted on a V-shaped groove with an opening angle of 120°. Further, each groove was formed by two blocks made of stainless steel 316 having non-round bottoms. The displacement of the pendulum was measured by a laser displacement sensor (IL-S025, Keyence Company) at the tip of the aluminum extension arm, with the distance from the fulcrum being 128 mm. The sensitivity of the thrust stand was calibrated by using a pulley and weight arrangement driven by a direct-current motor maintained at the same ambient pressure as that during the thruster operations. In addition, a "tare force," which is an apparent thrust that should be corrected in the thruster measurement, was measured beforehand as described in Ref. 30.

A double (electrostatic) probe was used for the measurement of electron temperature T_e and electron number density n_e. The probe tip was composed of two 0.3-mm-diameter tungsten wires with an effective length of 3 mm. The separation distance between the wires was 2.2 mm. A floating emissive probe was used for the plasma space potential V_s with respect to the cathode potential measurement. Further, a 0.185-mm-diameter wire fabricated by 1% thoriated tungsten was bent into a semicircular shape of diameter 2 mm and used for thermionic electron emission. In addition, the emission part was Joule-heated by supplying a heater current to emit a sufficient number of thermionic electrons. When a heater

current greater than 8.2 A was supplied, the probe floating voltage was saturated. The details of data processing, correction procedures, and error analysis are further described in Ref. 31.

IV. CRITERIA FOR HYBRID ION ACCELERATION

A. Location of the propellant injection port

In electrostatic ion acceleration, ions should be generated near the anode to utilize the applied voltage for efficient ion acceleration. Because the ionization frequency is proportional to neutral number density,[2] it is expected that increasing the neutral number density near the anode will enhance electron impact ionization specifically in the anode potential region. For the validation of the effect of this near anode injection method, we newly developed a thruster, schematically illustrated in Fig. 1. In thruster type-I, only a short portion of the inner surface of the ring anode with an inner diameter R_a ($= 40$ mm) and a length of 8 mm was exposed to the discharge channel as an effective anode. A slowly diverging magnetic field was applied using a water-cooled solenoid coil (inner diameter 100 mm, outer diameter 210 mm, and length 100 mm). B_c was varied with the changing current on the solenoid coil by using a commercial power supply (N8761A, Keysight Technologies). A commercial hollow cathode (LHC-03-AE1-01, Kaufman & Robinson Inc.) was set on the center axis with the axial location of its tip at the center of the solenoid coil. For the cathode operation,
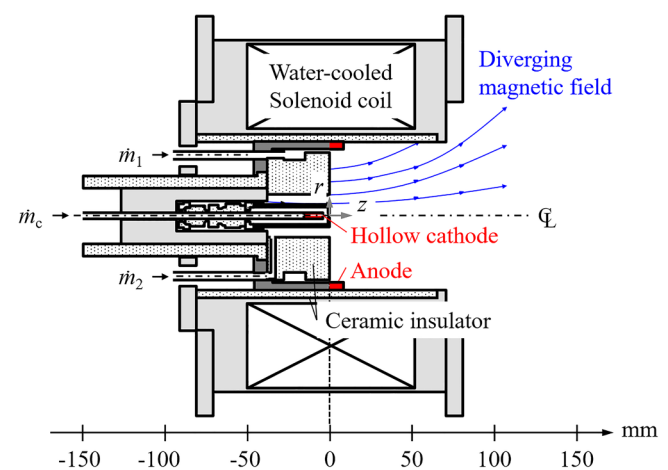

FIG. 1. Schematic of thruster type-I.

a commercial power supply (KC8002, Kaufman & Robinson Inc.) and mass flow controller (Model 3660, Kojima Instruments Inc., F.S. = 100 sccm) were used. The electrodes were assembled with a ceramic insulator made of alumina. Further, the thruster had two propellant injection ports: one was near the anode propellant injection wherein the propellant was injected along the inner surface of the anode via a 1.5-mm-thick annular slit. The other was near the cathode propellant injection wherein the propellant was injected along the outer surface of the keeper electrode (fabricated from tantalum, outer diameter 14 mm) via a 5.5-mm-thick annular slit. The slit width of the near cathode propellant injection was designed to maintain the same exit area of the near anode propellant injection slit. The flow rate of each injection port ($\dot{m}_1$ for the near anode injection and $\dot{m}_2$ for the near cathode injection) was independently controlled using two mass flow controllers (Model 3660, Kojima Instrument Inc., F.S. = 30 sccm). At $z = 75$ mm (the thruster exit plane), the cross-sectional area at the thruster exit S_{out} was 6.3×10^{-3} m^2.
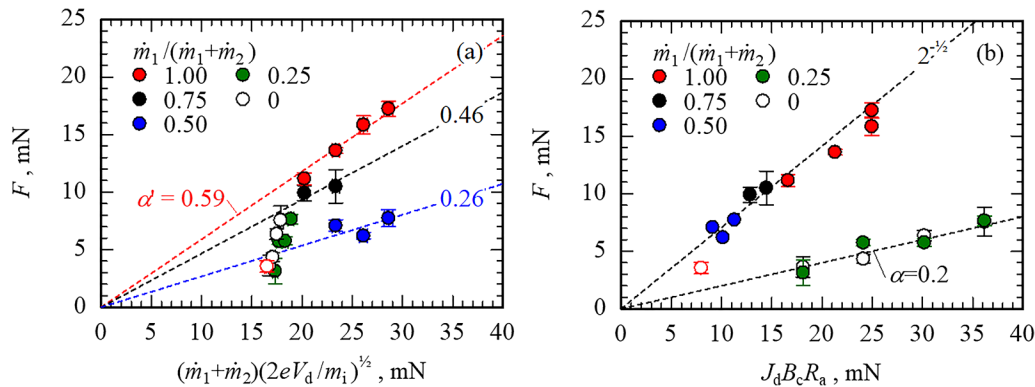
Figure 2 shows the V_d dependency of the mass-averaged exhaust velocity $F/(\dot{m}_1 + \dot{m}_2)$ and normalized discharge current
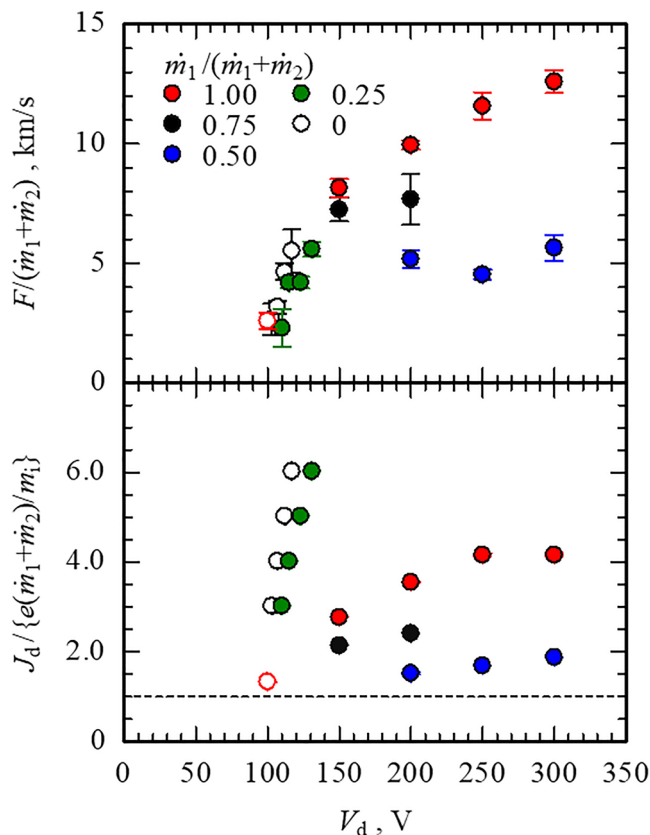
$J_d/\{e(\dot{m}_1 + \dot{m}_2)/m_i\}$ with different propellant injection ratios $\dot{m}_1/(\dot{m}_1 + \dot{m}_2)$, where e and m_i are elemental charge and ion mass, respectively. The total flow rate $\dot{m}_1 + \dot{m}_2$ was set to 1.4 mg/s (= 1.0 Aeq), and the flow ratio $\dot{m}_1/(\dot{m}_1 + \dot{m}_2)$ was changed from 0 (entire propellant was supplied through the cathode injection slit) to 1.0 (through the anode injection slit). The cathode flow rate $\dot{m}_c$ was fixed at 0.49 mg/s (= 0.36 Aeq). When $\dot{m}_1/(\dot{m}_1 + \dot{m}_2)$ was set to 0 and 0.25, the thruster operated in constant current mode, in which the discharge current is the setting value and the discharge voltage is the dependent variable, whereas when set to 0.50, 0.75, and 1.0, the constant voltage operation, in which that the discharge voltage is the setting value and the discharge current is the dependent variable, was achieved. Overall, $F/(\dot{m}_1 + \dot{m}_2)$ increased with increasing V_d and overlapped regardless of the propellant injection ratio, except in the case of $\dot{m}_1/(\dot{m}_1 + \dot{m}_2) = 0.5$. The maximum exhaust velocity was 12.6 km/s, equivalent to 1286 s of specific impulse I_{sp}. Regardless of the propellant injection ratio or constant current/voltage operation, $J_d/\{e(\dot{m}_1 + \dot{m}_2)/m_i\}$ increased with an increase in V_d. Further, when $\dot{m}_1/(\dot{m}_1 + \dot{m}_2)$ was set to 0 or 0.25 (constant current mode), V_d linearly increased with increasing $J_d/\{e(\dot{m}_1 + \dot{m}_2)/m_i\}$. In contrast when set to 0.50, 0.75, and 1.0 (constant voltage mode), $J_d/\{e(\dot{m}_1 + \dot{m}_2)/m_i\}$ gradually saturated with increasing V_d, particularly in the case of $\dot{m}_1/(\dot{m}_1 + \dot{m}_2) = 1.0$, wherein $J_d/\{e(\dot{m}_1 + \dot{m}_2)/m_i\} = 4.2$ at $V_d = 300$ V. Note that in the case where $\dot{m}_1/(\dot{m}_1 + \dot{m}_2) = 1.0$ with $V_d = 100$ V (plotted as an open red circle in Fig. 2), the experimental results, $F/(\dot{m}_1 + \dot{m}_2) = 2.6$ km/s, yielded the lowest level among all operating conditions. In the case where $V_d = 150$ V with $\dot{m}_1/(\dot{m}_1 + \dot{m}_2) = 1.0$, $F/(\dot{m}_1 + \dot{m}_2) = 8.1$ km/s, which is 3.1 times higher than that of the case where $V_d = 100$ V. Under the constant mass flow rate operation ($\dot{m}_1 + \dot{m}_2 = 1.4$ mg/s = 1.0 Aeq), this rapid velocity increment follows neither the velocity characteristics of electrostatic acceleration [$F/(\dot{m}_1 + \dot{m}_2)$ is proportional to $V_d^{1/2}$] nor those of electromagnetic acceleration [$F/(\dot{m}_1 + \dot{m}_2)$ is proportional to J_d]. In contrast, in the cases where $V_d \geq 150$ V, $F/(\dot{m}_1 + \dot{m}_2)$ increased gradually and a rapid increment was not observed. One possible reason for these lower values is insufficient propellant ionization,[32] which should be verified by ion beam current measurement. Therefore, the data points of $\dot{m}_1/(\dot{m}_1 + \dot{m}_2) = 1.0$ with $V_d = 100$ V are plotted as open red circles in Figs. 2 and 3 and are omitted in the following discussion.

The thrust characteristics of thruster type-I are shown in Figs. 3(a) and 3(b), which are roughly classified into two groups: constant-current operation with $\dot{m}_1/(\dot{m}_1 + \dot{m}_2) = 0$ and 0.25 or constant-voltage operation with $\dot{m}_1/(\dot{m}_1 + \dot{m}_2) = 0.50$, 0.75, and 1.0. Commonly, electrostatic-acceleration thrusters are operated in the constant-voltage mode where the discharge current is a variable dependent on V_d, whereas the electromagnetic-acceleration thrusters are operated in the constant-current mode where the discharge voltage is dependent on J_d. As shown in Fig. 3(a), the former group did not fit well to the electrostatic acceleration form of $(\dot{m}_1 + \dot{m}_2)(2eV_d/m_i)^{1/2}$. In contrast, as shown in Fig. 3(b), the thrust fit well to the electromagnetic-acceleration form of $J_d B_c R_a$, with the value of the coefficient α between 0.2 and 0.3. However, the latter group, $\dot{m}_1/(\dot{m}_1 + \dot{m}_2) = 0.50$, 0.75, and 1.0, had a thrust characteristic that fit well with both the electrostatic and electromagnetic-acceleration form; therefore, the electrostatic–magnetic hybrid acceleration appeared to occur in these cases. The coefficient of the electrostatic


FIG. 2. (color online). V_d dependency of $F/(\dot{m}_1 + \dot{m}_2)$ and $J_d/\{e(\dot{m}_1 + \dot{m}_2)/m_i\}$ with $\dot{m}_1 + \dot{m}_2 = 1.4$ mg/s (= 1.0 Aeq), $\dot{m}_c = 0.49$ mg/s (= 0.36 Aeq), and $B_c = 150$ mT. The open red circle [$\dot{m}_1/(\dot{m}_1 + \dot{m}_2) = 1.0$ with $V_d = 100$ V] is omitted in the following discussion.

FIG. 3. (color online). Thrust characteristics of thruster type-I with $\dot{m}_1 + \dot{m}_2 = 1.4$ mg/s (= 1.0 Aeq), $\dot{m}_c = 0.49$ mg/s (= 0.36 Aeq), and $B_c = 150$ mT; (a) electrostatic acceleration model and (b) electromagnetic acceleration model. The point shown as an open red circle [$\dot{m}_1/(\dot{m}_1 + \dot{m}_2) = 1.0$ with $V_d = 100$ V] is omitted from the discussions about the hybrid operation criteria.

acceleration α' depended on $\dot{m}_1/(\dot{m}_1 + \dot{m}_2)$ such that the higher propellant injection ratio showed a higher α' value. Moreover, the characteristics were consistent with the ion acceleration scenario in electrostatic–magnetic hybrid ion acceleration such that the propellant was ionized near the anode and then experienced the electrostatic acceleration between the potential drop from the anode to that on the center axis. In addition, the thrust characteristics of the latter group in the electromagnetic acceleration form exhibited no dependency on the propellant injection ratio and showed α value of 0.77. Fradkin et al.[28] assumed plasma in a hollow cylinder with inner and outer radii of R_c and R_a. respectively, which acted as a rigid rotator, in which the angular velocity was kept uniform at an axial location, and the rotational kinetic energy was fully converted into axial kinetic energy after expansion through a diverging

magnetic nozzle. In this model, an azimuthal torque is generated through a Lorentz force induced by the interaction between $\mathbf{J_d}$ and $\mathbf{B_a}$ both of which have only (z, r) component. Under these assumptions, the thrust is given in a closed form as

$$F = \frac{1}{\sqrt{2}} J_d B_a R_a \frac{1 - (R_c/R_a)^2}{\sqrt{1 + (R_c/R_a)^2}}$$
$$\simeq \frac{1}{\sqrt{2}} J_d B_a R_a \left\{ 1 - \frac{3}{2} \left(\frac{R_c}{R_a} \right)^2 \right\}. \quad (14)$$

In our experiment, $(R_c/R_a)^2 \approx 0.0025 \ll 1.0$ and we obtain $\alpha = 2^{-\frac{1}{2}}$, which is smaller than that of the presented result with
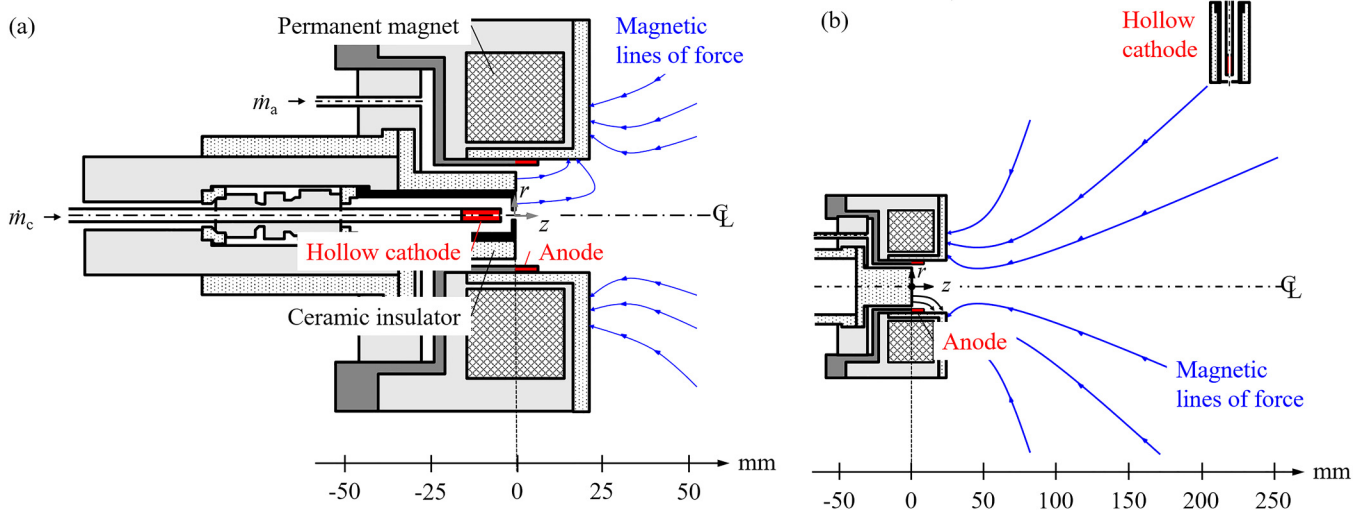
FIG. 4. Schematic of thruster type-II; (a) CC operation and (b) EC operation.

TABLE II. Permanent magnets used for different magnetic field strengths.

B_c, mT	Material	Inner diameter (mm)	Outer diameter (mm)	Length (mm)
210	Neodymium	58	98	30
315	Samarium-cobalt	45	100	30
402	Neodymium	45	100	30

$\dot{m}_1/(\dot{m}_1 + \dot{m}_2) = 0.50$, 0.75, and 1.0. Hereafter, the near anode propellant injection slit was employed in thruster types-II and III.

B. Relative cathode position with respect to the magnetic field

In the diverging magnetic field, the electron motion and electric field configuration are different from those in the electric field of a Hall thruster such that an axial electric field was maintained near the exit by the applied radial-magnetic field. In contrast, in the electrostatic–magnetic hybrid ion acceleration scheme, a radial potential drop is required under the diverging magnetic field, and the hollow cathode should be located on the center axis. In this section, we investigated the effect of the hollow cathode relative position with respect to the identical diverging magnetic field. By changing the hollow cathode position, central cathode (CC) or external cathode (EC), the thrust characteristics and plasma parameters (n_e, T_e, and V_s distributions) were evaluated.

To achieve this, we developed thruster type-II, schematically illustrated in Figs. 4(a) and 4(b) for CC and EC operation, respectively. As in thruster type-I, it also has a ring anode made of copper with an inner radius of $R_a = 15$ and 8 mm of the effective length. On the center axis, the same commercial hollow cathode with the in-house keeper electrode (fabricated from tantalum, 14 mm outer diameter) as that used in thruster type-I was located. Further, a ceramic insulator (Photoveel®, Ferrotec Ceramics Corporation, composed mainly of SiO_2 and Al_2O_3) was placed between the anode and the hollow cathode. The propellant was injected only along the anode inner surface via a 1.5-mm-thick annular slit between the anode inner surface and the ceramic insulator. An external magnetic field was applied using a permanent ring magnet, which was packed in a housing fabricated with stainless steel (ISO: 4401-316-00-I), which, in turn, was protected from plasma using a ceramic wall plate. To change the B_c value to 210, 315, and 420 mT, the size/material of the permanent ring magnet was changed as summarized in Table II. Further, the applied magnetic field had a cusp around the thruster exit over the ceramic wall plate. For the hollow cathode operation and near anode propellant injection, the same power supply and mass flow controllers were used as those described in thruster type-I. At $z = 23$ mm (the thruster exit plane), S_{out} was 0.9×10^{-3} m^2. Figure 4 shows a schematic of thruster type-II with EC operation [scale is not the same as in Fig. 4(a)]. The thruster head components were exactly the same as those used for thruster type-II with CC operation, except for the location of the hollow cathode. Instead of the central hollow cathode, an insulating plate made in Photoveel® was installed at the center of the thruster head. The cathode was located at $(z, r) = (220$ mm, 140 mm) where the magnetic field strength was less than 1 mT.

The thrust characteristics of thruster type-II with CC and EC operations are shown in Figs. 5(a) and 5(b). For comparison, the results of thruster type-I with $\dot{m}_1/(\dot{m}_1 + \dot{m}_2) = 1.0$ are plotted as well. From Fig. 5(a), it can be observed that the thrust coefficient of thruster type-II with CC operation is higher than that of thruster type-I; $\alpha' = 0.69$ for thruster type-II and 0.59 for thruster type-I with $\dot{m}_1/(\dot{m}_1 + \dot{m}_2) = 1.0$. However, in thruster type-II with EC operation, α' was calculated as 0.57. The thrust characteristics in the electromagnetic acceleration form are shown in Fig. 5(b), wherein thruster type-II with CC operation roughly fit to the linear relation of $J_d B_c R_a$ and the slope α ranged from 0.92 to 1.18. In EC operation, the thrust increased linearly with increasing $J_d B_c R_a$ and α was 2.0; however, the slope changed at approximately $J_d B_c R_a = 15$ mN and subsequently the thrust was not directly proportional to $J_d B_c R_a$. Hence, it should be noted that the thrust generation mechanism in EC operation changed at $J_d B_c R_a = 15$ mN, and for $J_d B_c R_a \leq 15$ mN, both electrostatic and electromagnetic ion
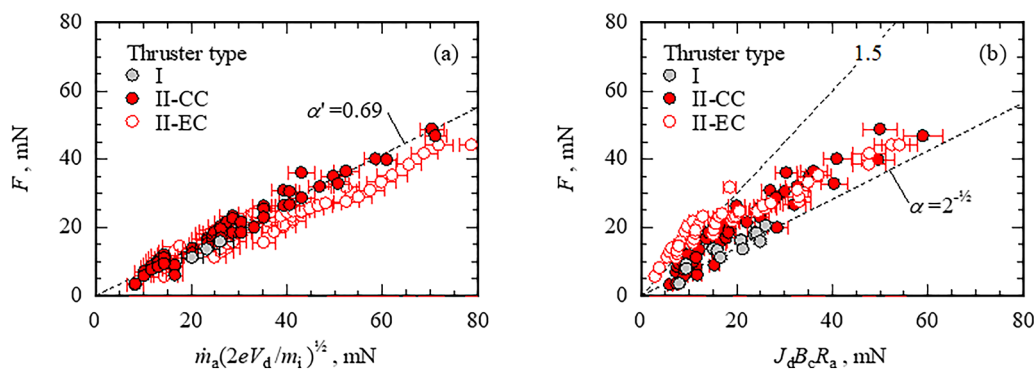
FIG. 5. Thrust characteristics of thruster type-II with $\dot{m}_c = 0.49$ mg/s (= 0.36 Aeq); (a) electrostatic acceleration model and (b) electromagnetic acceleration model. For comparison, the data of thruster type-I with $\dot{m}_1/(\dot{m}_1 + \dot{m}_2) = 1.0$ are also plotted.

accelerations contributed to generating thrust, whereas for $J_d B_c R_a \geq 15$ mN, the electrostatic acceleration was dominant. Therefore, the CC operation showed the electrostatic–magnetic hybrid ion acceleration, whereas the EC operation showed the hybrid acceleration in limited cases and was primarily dominated by the electrostatic ion acceleration. The reason for the difference will be discussed with reference to electron Hall parameters later.

The plasma parameters were measured using the double probe, and the emissive probe was used under identical operating conditions ($\dot{m}_a = 1.4$ mg/s = 1.0 Aeq, $\dot{m}_c = 0.48$ mg/s = 0.36 Aeq, $B_c = 315$ mT, $V_d = 250$ V) except for the hollow cathode position (CC or EC). The distributions of n_e, T_e, and V_s are shown in Figs. 6(a)–6(c), respectively, and the upper half presents the distributions of CC operation while the lower half is that of EC operation. A separatrix of the applied magnetic field roughly existed near $z \approx 25$ mm.

From Fig. 6(a), it can be observed that the high-density region is located in the vicinity of the hollow cathode exit for CC operation, whereas in EC operation, such a high-density region is not observed, and the generated plasma is confined within $z \leq 25$ mm. Further, from Fig. 6(b), the high electron temperature region is found to be concentrated in the vicinity of the anode in CC operation. In EC operation, T_e is not distributed along the magnetic lines of force and instead shows locally higher values. The space potential distribution shown in Fig. 6(c) is different for the cathode position. Moreover, in CC operation, the magnetic field configuration strongly affected the V_s distribution such that V_s had a constant value along the magnetic lines of force as well as Hall thrusters. In contrast, in EC operation, the magnetic field separatrix affected the distribution of V_s similar to how it did in the n_e distribution. The high potential region was confined within $z \leq 25$ mm and then gradually decreased toward downstream, which is commonly observed in cylindrical Hall thrusters, high-efficiency multistage plasma thrusters, and cusped-field thrusters.

The axial distributions of n_e, T_e, and V_s on the center axis are shown in Fig. 7(a). In CC operation, the highest n_e value of 2.5×10^{19} m^{-3} was observed at $(z, r) = (5$ mm, 0 mm), which then monotonically decreased in the downstream region. In EC operation, n_e was maintained in the order of 10^{18} m^{-3} in $z \leq 25$ mm; however, beyond $z = 25$ mm, n_e quickly decreased in the downstream region. The T_e and V_s values of CC operation were maintained at the lower level along the center axis. Along the central axis, T_e was found to be less than 4.5 eV, and V_s decreased from 40 V at $(z, r) = (5$ mm, 0 mm) to 20 V at $(z, r) = (100$ mm, 0 mm), which was close to the keeper voltage of 16 V. In EC operation, T_e showed locally higher values up to 25 eV at $(z, r) = (10$ mm, 0 mm). The high T_e region was concentrated in the 5 mm $\leq z \leq 25$ mm region and in other regions, T_e remained at approximately 5 eV. Further, in $z \leq 25$ mm, V_s was greater than 160 V; however, beyond $z = 25$ mm, V_s quickly decreased monotonically in the downstream region and an axial electric field was observed.

Figure 7(b) shows radial distributions of n_e, T_e, and V_s at $z = 5$ mm. In both the cathode positions, higher n_e values were observed on the center axis than that of the near anode. The T_e value in CC operation reached a higher value close to the anode inner surface ($r = 15$ mm) and reached 12 eV at $(z, r) = (5$ mm, 12.5 mm). In EC operation, T_e, and V_s did not exhibit significant changes as T_e ranged from 7.6 to 14 eV, and V_s increased from 175 V at $(z, r) = (5$ mm, 0 mm) to 200 V at $(z, r) = (5$ mm,
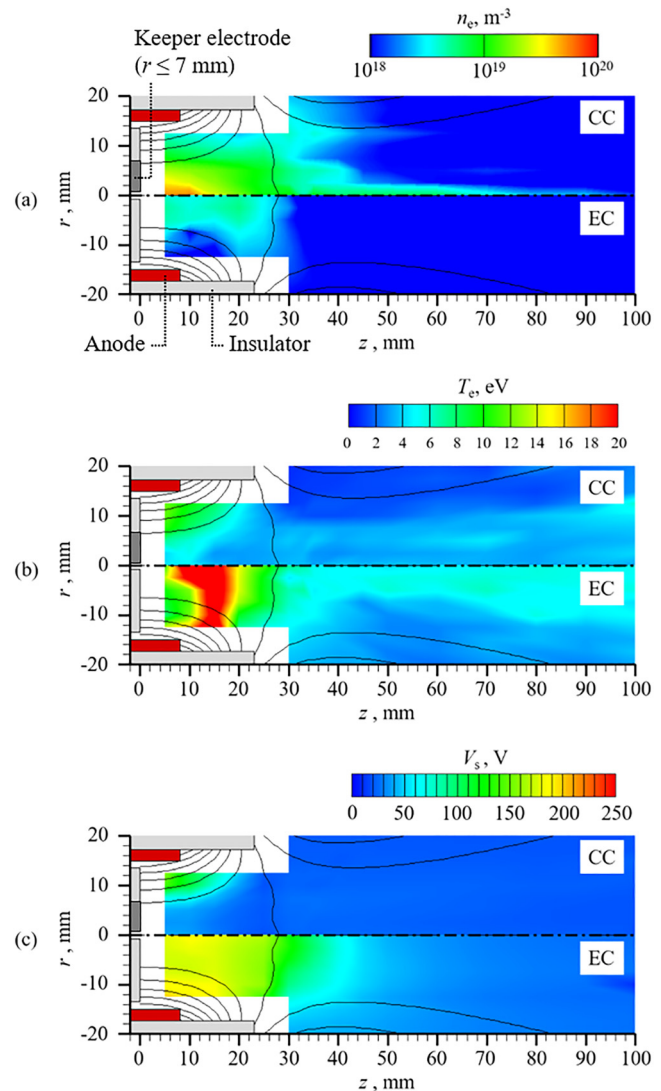
FIG. 6. Distributions of (a) n_e, m^{-3}, (b) T_e, eV, and (c) V_s, V in thruster type-II with $\dot{m}_a = 1.4$ mg/s (1.0 Aeq), $\dot{m}_c = 0.49$ mg/s (= 0.36 Aeq), $B_c = 315$ mT, $V_d = 250$ V; upper half and lower half are for CC and EC operations, respectively.

12.5 mm). However, in CC operation, V_s increased quickly toward the anode from 40 V at $(z, r) = (5$ mm, 0 mm) to 200 V at $(z, r) = (5$ mm, 12.5 mm). Subsequently, using the n_e and T_e values at $(z, r) = (5$ mm, 0 mm), the electron Hall parameter was calculated. Here, only Coulomb collisions were considered while calculating the electron collision frequency.[2] The calculated electron Hall parameter was 55 for CC operation and 3140 for EC operation. Thus, because of the small Hall parameter, electrons were well thermalized and a constant T_e and V_s were observed along the magnetic lines of force in CC operation. Here, note that the inside plug-wall potential (namely, the boundary condition of the V_s
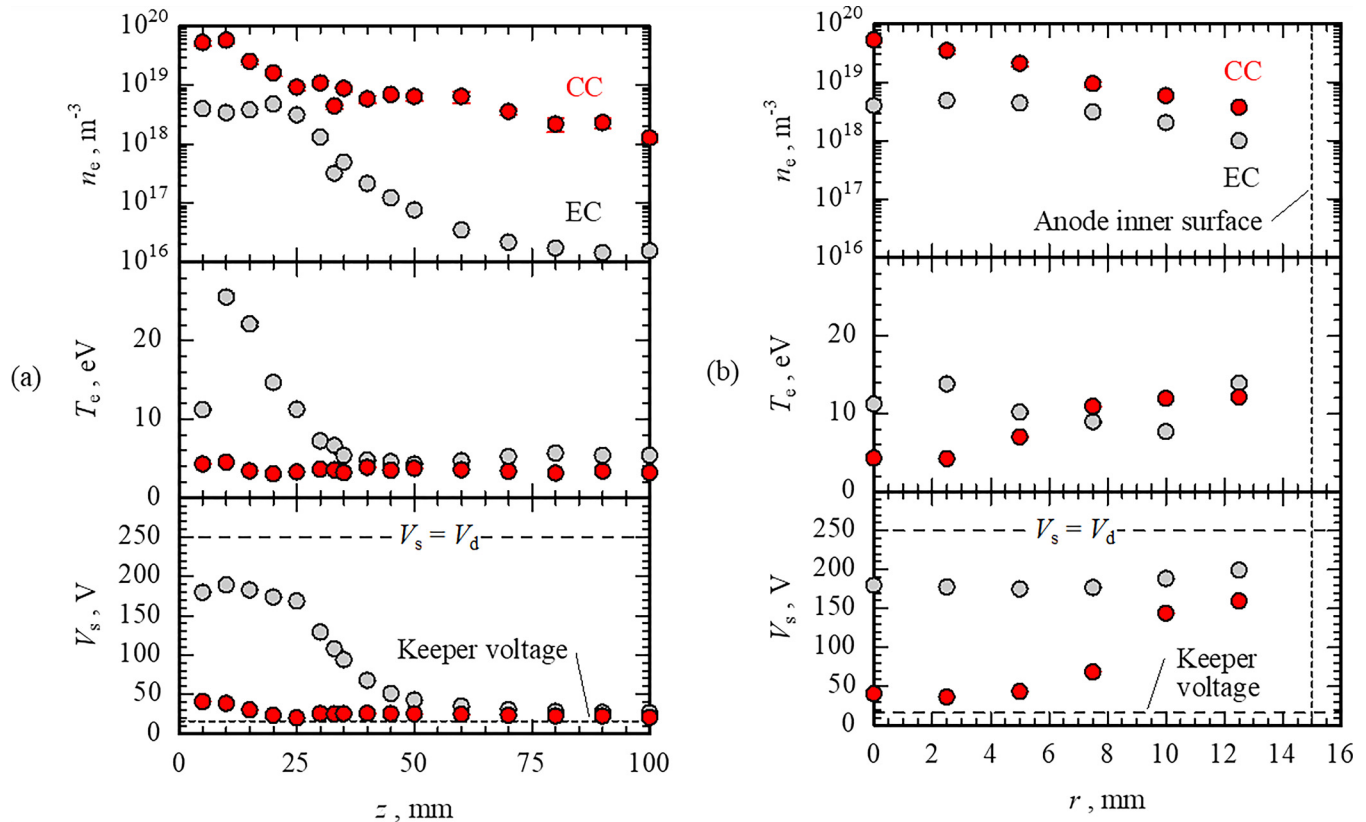
FIG. 7. Distribution of plasma parameters of thruster type-II with the same operating condition in Fig. 6; (a) axial distribution on center axis and (b) radial distribution on $z = 5$ mm.

distribution) was different between the cases of CC/EC operations. In CC operation, the wall potential in $r < 7$ mm was equal to the keeper voltage ($= 16$ V) and in 7 mm $< r \leq 13.5$ mm, the wall potential was equal to the floating potential [calculated as 80–95 V from the T_e and V_s values shown in Fig. 7(b)]. In EC operation, the plug-wall potential in $r \leq 13.5$ mm was equal to the floating potential [calculated as 104–147 V from the T_e and V_s values shown in Fig. 7(b)]. These are the upstream-boundary conditions of the space potential distribution in CC/EC operations. However, the effect of wall potential was limited within the sheath length and the electric potential in the bulk plasma was dominated by the electron Hall parameter. Therefore, even with the different upstream-boundary conditions between CC/EC operations, the electrical potential distributions and thruster performances should not be different from the presented data. As described in Sec. III A, the radial electric field for realizing electrostatic–magnetic hybrid acceleration scheme was maintained only in CC operation case, which is consistent with the thrust characteristics shown in Fig. 5.

In summary, we experimentally obtained two design criteria to achieve the hybrid ion acceleration: (i) near anode propellant injection and (ii) on-axis hollow cathode location. Injecting xenon propellant along the inner surface of the anode enhances the

electron impact ionization and generates ions that are electrostatically accelerated through the radial-inward potential gradient along the axial magnetic lines of force. As a result, the thrust coefficient α in the hybrid ion acceleration scheme exceeded that of the conventional swirl acceleration model.

V. HIGH-THRUST-DENSITY OPERATION

Following the thruster design criteria described in Sec. IV, a type-III thruster was developed to demonstrate the high-thrust-density operation by electrostatic–magnetic hybrid ion acceleration. In addition, our previous work showed that strengthening the magnetic field, particularly near the anode, enhanced near anode ionization, and the generated ions enabled utilization of the potential drop between the electrodes for efficient electrostatic ion acceleration. Following the magnetic field enhancement on anode, we newly developed the thruster type-III, schematically illustrated in Fig. 8.

Thruster type-III has features similar to those of thruster type-II; it has a commercial hollow cathode (LHC-03-AE1-01, Kaufman & Robinson Inc.) on the center axis and a ring anode placed coaxially around the cathode. Between the anode and
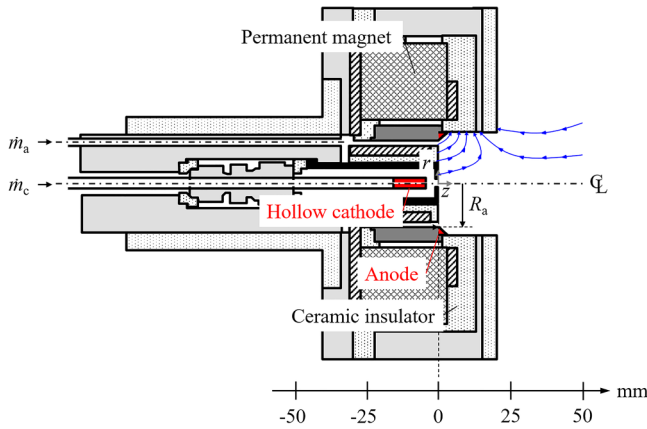
FIG. 8. Schematic of thruster type-III.

cathode, a ceramic (Photoveel) insulator was installed. An external magnetic field was applied using a permanent ring magnet made of samarium-cobalt (as described in Table II). Further, at the front and back surfaces of the magnet, magnetic yokes made of soft iron were mounted to strengthen the magnetic field (particularly near the anode) to enhance the near-anode ionization.[33] The magnetic field strength at $(z, r) = (0$ mm, $R_a)$ was 590 mT, while B_c was 270 mT. The copper-made ring anode had a tilted inner surface roughly relative to the magnetic field lines of force. In addition, the anode inner radius R_a was 15 mm, and the effective length was 3 mm with the inner angle of 45°. The propellant was fed through a 1.5-mm slit between the inner surface of the anode and the ceramic insulator. For the hollow cathode operation and near anode propellant injection, the power supply and mass flow controllers as described in thruster type-I were used.

The operation characteristics of thruster type-III are shown in Fig. 9. For comparison, those of thruster type-I and type-II with CC operation are plotted as well. With an increase in V_d, $F/\dot{m}_a$ in thruster type-III increased and gradually saturated at approximately $V_d = 400$ V. For $V_d \leq 300$ V, thruster type-III showed a lower value of $F/\dot{m}_a$ than that of thruster types-I and II with CC operation; the maximum $F/\dot{m}_a$ at $V_d = 300$ V were 15, 17, and 13 km/s for thruster types-I and II with CC operation and III, respectively. However, thruster type-III showed a completely different V_d dependency of $J_d/(e\dot{m}_a/m_i)$; that is, on increasing V_d, $J_d/(e\dot{m}_a/m_i)$ maintained a constant level of 2.0, whereas in the case of thruster types-I and II with CC operation, it increased. This is because of the strong magnetic field that trapped the electrons along the magnetic lines of force and thereby suppressed the electron diffusion across the magnetic lines of force. In addition, the anode inner surface of thruster type-III was tilted (see Fig. 8); thus, no magnetic lines of force were terminated at the anode inner surface and electrons could not directly flow into the anode.

The thrust characteristics of the electrostatic acceleration model and the electromagnetic acceleration model are shown in Figs. 10(a) and 10(b), respectively. As shown in Fig. 10(a), the obtained thrust fit well to the electrostatic ion acceleration form.
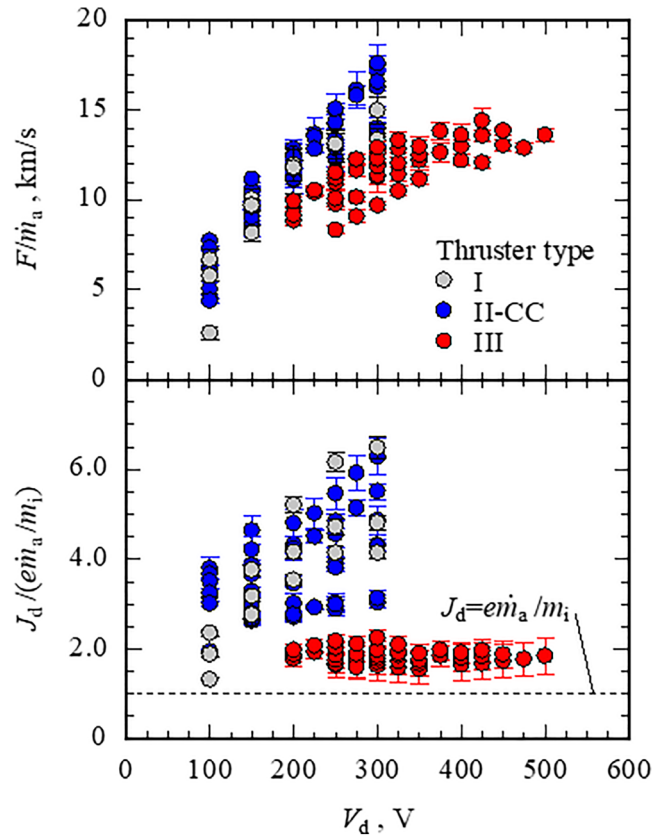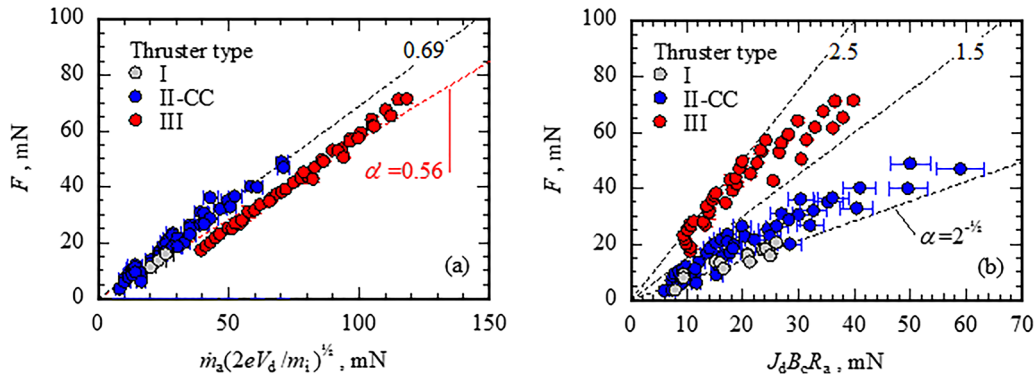

FIG. 9. V_d dependency of $F/\dot{m}_a$ and $J_d/(e\dot{m}_a/m_i)$ with $\dot{m}_c = 0.49$ mg/s (= 0.36 Aeq). For comparison, the data of thruster type-I with $\dot{m}_1/(\dot{m}_1 + \dot{m}_2) = 1.0$ and that of thruster type-II with CC operation are also plotted.

The coefficient α' (= 0.56) is close to that of thruster types-I and II with CC operation. Further, in the thrust characteristics in the electromagnetic acceleration form shown in Fig. 10(b), the thrust roughly fit to the linear relation of $J_dB_cR_a$ as well as thruster types-I and II with CC operation; however, its coefficient α (which ranged from 1.5 to 2.5) was much higher than those of the other thruster types. There are two possible reasons for this increment; one is enhanced propellant ionization near the anode and consequently, an increment in the ion beam energy due to the strengthened magnetic field on the anode described above. Another reason is that the multi-charged ions generate thrust larger than that of the singly charged ions because the electrostatic thrust is proportional to the square root of the charge state. The discharge voltage (≥ 200 V) well exceeded the xenon-propellant ionization voltage (12.1 and 21.2 V for single and double ionization, respectively[34]), and both factors can contribute to increasing α. To break down the contributions from the two factors, ion beam characteristics (propellant utilization and current fractions from each charge-state ion) must be further investigated.

The thrust density F/S_{out}, thrust efficiency η_a ($\equiv F^2/(2\dot{m}_a J_d V_d)$), and thrust-to-power ratio F/P_a in electrostatic–magnetic hybrid ion

FIG. 10. Thrust characteristics of thruster type-III with $\dot{m}_c$ = 0.49 mg/s (= 0.36 Aeq); (a) electrostatic acceleration model and (b) electromagnetic acceleration model. For comparison, the data of thruster type-I with $\dot{m}_1/(\dot{m}_1 + \dot{m}_2)$ = 1.0 and that of thruster type-II with CC operation are also plotted.

accelerations are shown in Fig. 11. The horizontal axis represents the propellant mass flux $\dot{m}_a/S_{out}$. Regardless of the thruster types, higher $\dot{m}_a/S_{out}$ yielded a larger F/S_{out}. The largest thrust density of 70 N/m² with 1200 s of $I_{sp,a}$ was obtained by thruster type-III at 4400 Aeq/m² (= 6.0×10^{-3} kg/s/m²) of $\dot{m}_a/S_{out}$. Because of the strong magnetic field in thruster type-III, electron cross-field transport was suppressed, and stable operation was achieved even with the higher propellant mass flux. Thus, the thrust efficiency and the corresponding thrust-to-power ratio did not exhibit strong dependency on the propellant mass flux and ranged within 10%–18% for η_a and 26–34 mN/kW for F/P_a.

Next, these values of thruster type-III were compared to those of the Hall thruster. To estimate $\dot{m}_a/S_{out}$, F/S_{out}, η_a, and $I_{sp,a}$ for the typical Hall thruster, a scaling law derived from experimentally obtained 1-kW-class 18 Hall thrusters was used as a reference value.[35] In Hall thruster operation, $\dot{m}_a/S_{out}$ should be 0.9×10^{-3} kg/s/m² to ensure a stable plasma discharge and an efficient thruster operation. However, because $\dot{m}_a/S_{out}$ is uniquely decided, F/S_{out} and $I_{sp,a}$ are proportional only to $(V_d)^{1/2}$. For the same $I_{sp,a}$ value (~1200 s), V_d, F/S_{out}, and η_a were calculated as 174 V, 11 N/m², and 45%, respectively, using the coefficients of thruster geometry, mass flow rate, thrust, and discharge power. In this study, a stable operation was achieved for $\dot{m}_a/S_{out} \leq 6.1 \times 10^{-3}$ kg/s/m², and a decrement in η_a was not observed. Owing to this high mass flux, the thrust density increased up to 6.3 times higher than the scaled value for Hall thrusters. In terms of multi-mode (large thrust/high specific impulse) operation,[3] the high thrust-density operation would be useful for the large thrust mode. For high specific impulse mode,[36] the violent plasma oscillations caused by a neutral depression[37] were not observed even with increased V_d (≤500 V). Therefore, the presented thruster also exhibited a capability for stable, high-specific-impulse operation. In spite of these advantages, however, the thrust efficiency and corresponding thrust-to-power ratio should be improved. One possible approach is scaling up both thruster size and input power.[32] To determine the reason for the lower thrust efficiency, a
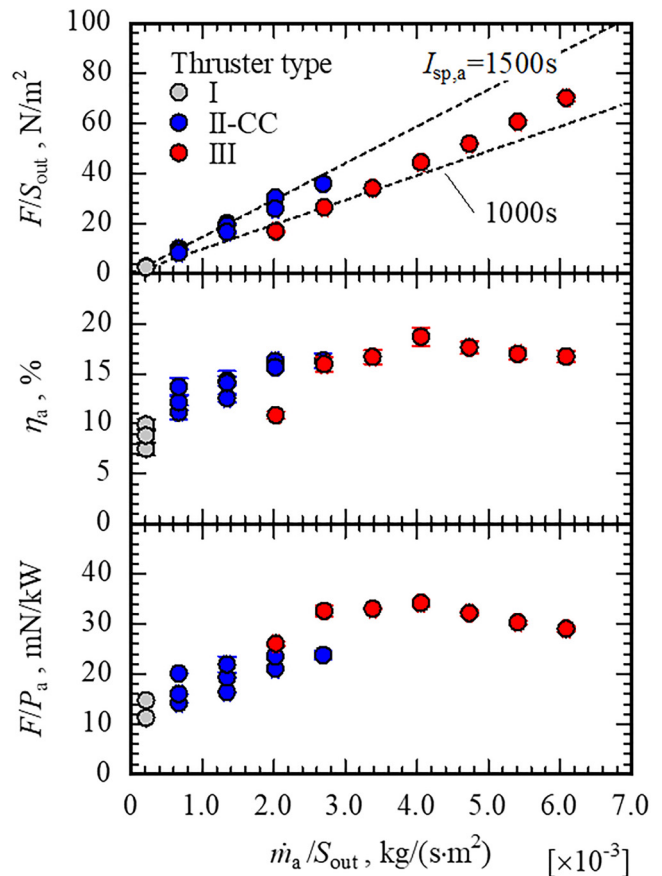
FIG. 11. $\dot{m}_a/S_{out}$ dependency of F/S_{out} and η_a with $\dot{m}_c$ = 0.49 mg/s (= 0.36 Aeq) and V_d = 250 V. For comparison, the data of thruster type-I with $\dot{m}_1/(\dot{m}_1 + \dot{m}_2)$ = 1.0 and that of thruster type-II with CC operation are also plotted.

dataset of both plasma parameters (n_e, T_e, and V_s distributions) and efficiencies (propellant/current utilization, beam energy, and beam divergence) is required, which is beyond the scope of this study and warrants further investigation.

VI. CONCLUSION

We investigated thrust characteristics using three thrusters (types-I, II, and III), comprising a slowly diverging magnetic field between an on-axis hollow cathode and a coaxially set ring anode. To achieve an electrostatic–magnetic hybrid ion acceleration, we proposed two experimentally obtained criteria regarding near-anode propellant injection and the on-axis hollow cathode location by using thruster type-I and type-II, respectively, such that the propellant injected along the inner surface of the anode is ionized near the anode and accelerated through the applied potential drop in the radial-inward direction. From the plasma diagnostics inside and outside the discharge channel, the electron Hall parameter was found to be up to 55 in the investigated region when the cathode was located at the center axis, and the electrons are expected to be thermalized well through Coulomb collisions. Therefore, the potential gradient along the magnetic lines of force was observed. The measured thrust exhibited both electrostatic and electromagnetic acceleration characteristics and fit well with the thrust formula derived for steady-state and quasi-neutral plasma flows. To demonstrate high-thrust-density-operation, thruster type-III was developed, following the above-mentioned design criteria. It was found that by increasing propellant mass flux, the thrust density increased up to 70 N/m^2 without violent plasma oscillations. Compared to a scaled model of Hall thrusters, the thrust density was higher by a factor of 6.3 for an identical specific impulse of 1200 s. Beside those advantages, however, the results of lower thrust efficiency (up to 18%) warrant further investigations in both plasma parameters and ion beam characteristics.

ACKNOWLEDGMENTS

AUTHOR DECLARATIONS

Conflict of Interest

The authors have no conflicts to disclose.

DATA AVAILABILITY

The data that support the findings of this study are available from the corresponding author upon reasonable request.

REFERENCES

[1]K. Holste, P. Dietz, S. Scharmann, K. Keil, T. Henning, D. Zschätzsch, M. Reitemeyer, B. Nauschütt, F. Kiefer, F. Kunze, J. Zorn, C. Heiliger, N. Joshi, U. Probst, R. Thüringer, C. Volkmar, D. Packan, S. Peterschmitt,

K.-T. Brinkmann, H.-G. Zaunick, M. H. Thoma, M. Kretschmer, H. J. Leiter, S. Schippers, K. Hannemann, and P. J. Klar, "Ion thrusters for electric propulsion: Scientific issues developing a niche technology into a game changer," Rev. Sci. Instrum. **91**, 061101 (2020).
[2]D. M. Goebel and I. Katz, *Fundamentals of Electric Propulsion: Ion and Hall Thrusters* (John Wiley & Sons, 2008).
[3]I. Funaki, S. Cho, T. Sano, T. Fukatsu, Y. Tashiro, T. Shiiki, Y. Nakamura, H. Watanabe, K. Kubota, Y. Matsunaga, and K. Fuchigami, "Development of a 6-kW-class Hall thruster for geostationary missions," Acta Astronaut. **170**, 163–171 (2020).
[4]K. Takahashi, C. Charles, R. W. Boswell, and A. Ando, "Demonstrating a new technology for space debris removal using a bi-directional plasma thruster," Sci. Rep. **8**, 014417 (2018).
[5]F. C. Díaz, J. Carr, L. Johnson, W. Johnson, G. Genta, and P. F. Maffione, "Solar electric propulsion for human Mars missions," Acta Astronaut. **160**, 183–194 (2019).
[6]K. Sankaran, L. Cassady, A. D. Kodys, and E. Y. Choueiri, "A survey of propulsion options for cargo and piloted missions to Mars," Ann. N.Y. Acad. Sci. **1017**, 450–467 (2004).
[7]G. Krülle, M. A. Kurtz, and A. Sasoh, "Technology and application aspects of applied field magnetoplasmadynamic propulsion," J. Propul. Power **14**, 754–763 (1998).
[8]R. R. Hofer and T. M. Randolph, "Mass and cost model for selecting thruster size in electric propulsion systems," J. Propul. Power **29**, 166–177 (2013).
[9]R. Jahn, *Physics of Electric Propulsion* (McGraw–Hill, New York, 1968), Chap. 6–8.
[10]F. F. Chen, *Introduction to Plasma Physics and Controlled Fusion*, 2nd ed. (Plenum Press, New York, 1984), Sec. 8.2.4.
[11]J. S. Snyder, D. M. Goebel, R. R. Hofer, J. E. Polk, N. C. Wallace, and H. Simpson, "Performance evaluation of the T6 ion engine," J. Propul. Power **28**, 371–379 (2012).
[12]J. B. Beattie and J. N. Matossian, "Xenon ion sources for space applications," Rev. Sci. Instrum. **61**, 348–353 (1990).
[13]J. P. Boeuf, "Tutorial: Physics and modeling of Hall thrusters," J. Appl. Phys. **121**, 011101 (2017).
[14]A. Smirnov, Y. Raitses, and N. J. Fisch, "Experimental and theoretical studies of cylindrical Hall thrusters," Phys. Plasmas **14**, 057106 (2007).
[15]T. Brandt, R. Schneider, J. Duras, D. Kahnfeld, F. G. Hey, H. Kersten, F. Jansen, and C. Braxmaier, "Particle-in-cell simulation of a down-scaled HEMP thruster," Trans. JSASS Aerospace Tech. Jpn. **14**, 235–242 (2016).
[16]S. Harada, T. Baba, A. Uchigashima, S. Yokota, A. Iwakawa, A. Sasoh, T. Yamazaki, and H. Shimizu, "Electrostatic acceleration of helicon plasma using a cusped magnetic field," Appl. Phys. Lett. **105**, 194101 (2014).
[17]Y. Raitses and N. J. Fisch, "Parametric investigations of a nonconventional Hall thruster," Phys. Plasmas **8**, 2579–2586 (2001).
[18]N. M. Tenenbaum, Q. Pratt, M. Nakles, N. Pilgram, M. Holmes, and W. Hargus, Jr., "Background pressure effects on Ion velocity distributions in an SPT-100 Hall thruster," J. Propul. Power **35**, 403–412 (2019).
[19]S. J. Hall, B. A. Jorns, S. E. Cusson, A. D. Gallimore, H. Kamhawi, P. Y. Peterson, T. W. Haag, J. A. Mackey, M. J. Baird, and J. H. Gilland, "Performance and high-speed characterization of a 100-kW nested Hall thruster," J. Propul. Power (in press) (2021).
[20]H. Li, Y. Wu, M. Ding, Y. Ding, L. Wei, D. Yu, and X. Wnag, "Discharge characteristics of a kilowatt Hall effect thruster with a variable channel," Vacuum **153**, 291–299 (2018).
[21]K. Dannenmayer and S. Mazouffre, "Elementary scaling relations for Hall effect thrusters," J. Propul. Power **27**, 236–245 (2011).
[22]A. M. Ortega, A. Guglielmi, F. Gaboriau, C. Boniface, and J. P. Boeuf, "Experimental characterization of ID-Hall, a double stage Hall thruster with an inductive ionization stage," Phys. Plasmas **27**, 023518 (2020).
[23]T. R. Nada, "Performance characterization of MPD thrusters," Aeronaut. J. **111**, 443–452 (2007).
[24]A. Sasoh, "Generalized Hall acceleration," J. Propul. Power **10**, 251–254 (1994).

[25]G. W. Butler and R. J. Cassady, "Directions for Arcjet Technology Development," J. Propul. Power **12**, 1026–1034 (1996).

[26]A. Sasoh, K. Mizutani, and A. Iwakawa, "Electrostatic/magnetic ion acceleration through a slowly diverging magnetic nozzle between a ring anode and an on-axis hollow cathode," AIP Adv. **7**, 065204 (2017).

[27]A. Sasoh, H. Kasuga, Y. Nakagawa, T. Matsuba, D. Ichihara, and A. Iwakawa, "Electrostatic-magnetic-hybrid thrust generation in central–cathode electrostatic thruster (CC–EST)," Acta Astronaut. **152**, 137–145 (2018).

[28]D. B. Fradkin, A. W. Blackstock, D. J. Roehling, T. F. Stratton, M. Williams, and K. W. Liewer, "Experiments using a 25–kW hollow cathode lithium vapor MPD Arcjet,"" AIAA J. **8**, 886–894 (1970).

[29]A. Sasoh, Ph.D. thesis, University of Tokyo, Tokyo, 1989.

[30]D. Ichihara, T. Uno, H. Kasuga, H. Kataoka, J. Jeong, A. Iwakawa, and A. Sasoh, "Ten-ampere-level, applied-field-dominant operation in magnetoplasmadynamic thrusters," J. Propul. Power **33**, 360–369 (2017).

[31]D. Ichihara, Y. Nakagawa, A. Iwakawa, and A. Sasoh, "Central and external cathode operations in a diverging-magnetic-field electrostatic thruster," J. Propul. Power **36**, 68–77 (2020).

[32]R. W. Conversano, D. M. Goebel, R. R. Hofer, I. G. Mikellides, and R. E. Wirz, "Performance analysis of a low-power magnetically shielded Hall thruster: Experiments," J. Propul. Power **33**, 975–983 (2017).

[33]D. Ichihara, A. Iwakawa, and A. Sasoh, "Effects of magnetic field profile near anode on ion acceleration characteristics of a diverging magnetic field electrostatic thruster," J. Appl. Phys. **122**, 043302 (2017).

[34]A. A. Sorokin, L. A. Shmaenok, S. V. Bobashev, B. Möbus, M. Richter, and G. Ulm, "Measurements of electron-impact ionization cross sections of argon, krypton, and xenon by comparison with photoionization," Phys. Rev. A **61**, 022723 (2000).

[35]E. Lee, Y. Kim, H. Lee, H. Kim, G. Doh, D. Lee, and W. Choe, "Scaling approach for sub-kilowatt Hall-effect thrusters," J. Propul. Power **35**, 1073–1079 (2019).

[36]R. R. Hofer, R. S. Jankovsky, and A. D. Gallimore, "High-specific impulse Hall thrusters, part 1: Influence of current density and magnetic field," J. Propul. Power **22**, 721–731 (2006).

[37]V. Giannetti, M. M. Saravia, and T. Andreussi, "Measurement of the breathing mode oscillations in Hall thruster plasmas with a fast-diving triple Langmuir probe," Phys. Plasmas **27**, 123502 (2020).